# Oligogenic heterozygous inheritance of sperm abnormalities in

2 mouse

- 3 Guillaume Martinez<sup>1,2,\*</sup>, Charles Coutton<sup>1,2</sup>, Corinne Loeuillet<sup>1</sup>, Caroline Cazin<sup>1,3</sup>, Jana
- 4 Muroňová<sup>1</sup>, Magalie Boguenet<sup>1</sup>, Emeline Lambert<sup>1</sup>, Magali Dhellemmes<sup>1</sup>, Geneviève
- 5 Chevalier<sup>1</sup>, Jean-Pascal Hograindleur<sup>1</sup>, Charline Vilpreux<sup>1</sup>, Yasmine Neirijnck<sup>4</sup>, Zine-Eddine
- 6 Kherraf<sup>1,3</sup>, Jessica Escoffier<sup>1</sup>, Serge Nef<sup>4</sup>, Pierre F. Ray<sup>1,3</sup>, Christophe Arnoult<sup>1,5,\*</sup>
- <sup>1</sup>Institute for Advanced Biosciences, INSERM, CNRS, Université Grenoble Alpes, F-38000
- 8 Grenoble

16

17

1

- 9 <sup>2</sup>UM de Génétique Chromosomique, Hôpital Couple-Enfant, CHU Grenoble Alpes, F-38000
- 10 Grenoble, France
- <sup>3</sup>UM GI-DPI, CHU Grenoble Alpes, F-38000 Grenoble, France
- <sup>4</sup>Department of Genetic Medicine and Development, University of Geneva Medical School,
- 13 Geneva 1211, Switzerland
- <sup>5</sup>Station de Primatologie, UPS 846, CNRS, F-13790 Rousset, France
- \*Correspondence: gmartinez@chu-grenoble.fr and christophe.arnoult@univ-grenoble-alpes.fr

## **ABSTRACT**

Male infertility is an important health concern that is expected to have a major genetic etiology. Although high-throughput sequencing has linked gene defects to more than 50% of rare and severe sperm anomalies, less than 20% of common and moderate forms are explained. We hypothesized that this low success rate could at least be partly due to oligogenic defects – the accumulation of several rare heterozygous variants in distinct, but functionally connected, genes. Here, we compared fertility and sperm parameters in male mice harboring one to four heterozygous truncating mutations of genes linked to multiple morphological anomalies of the flagellum (MMAF) syndrome. Results indicated progressively deteriorating sperm morphology and motility with increasing numbers of heterozygous mutations. This first evidence of oligogenic inheritance in failed spermatogenesis strongly suggests that oligogenic heterozygosity could explain a significant proportion of asthenoteratozoospermia cases. The findings presented pave the way to further studies in mice and man.

## MAIN TEXT

33

34

35

36

37

38

39

40

41

42

43

44

45

46

47

48

49

50

51

52

53

54

55

56

57

Infertility is a major health concern affecting 15% of couples of reproductive-age worldwide<sup>1,2</sup>. The infertility burden has increased globally for both genders in the past 30 years<sup>3</sup>, and now affects approximately 50 million couples worldwide<sup>4</sup>. Infertility is broadly treated by assisted reproductive technologies (ART), and today the number of individuals who were conceived by ART is close to 0.1% of the total world population, with over 8 million children already born following in vitro fertilization (IVF). Currently, ART is estimated to account for 1–6% of births in most countries<sup>5</sup>, with over 2.5 million cycles performed every year, resulting in over 500,000 births worldwide annually<sup>6</sup>. Despite this undeniable success, almost half the couples who seeks medical assistance for infertility fail to achieve successful pregnancy, and nearly 40% of infertile couples worldwide are simply diagnosed with unexplained or idiopathic infertility<sup>7</sup>. In the clinical context, few efforts are currently being made to understand and specifically address the underlying causes of a couple's infertility because ART, as a palliative treatment, can often successfully rescue fertility even without a molecular diagnosis. Nevertheless, this absence of identification of the causes of infertility means that we lack alternative treatments for couples for whom current therapies are unsuccessful. Consequently, it is essential to improve the molecular diagnosis of infertility. Human male infertility is a clinically heterogeneous condition with a complex etiology, in which genetic defects play a significant role. It is estimated that half of idiopathic cases of male infertility could be attributed to an as-yet unidentified genetic defect8. However, characterization of the molecular causes of male infertility represents a significant challenge, as over 4000 genes are thought to be involved in sperm production<sup>9</sup>. Over the past decade, significant progress has been made in gene identification thanks to the emergence of nextgeneration sequencing (NGS), and in functional gene validation thanks to new gene-editing techniques such as CRISPR/Cas9. NGS provides an inexpensive and rapid genetic approach

59

60

61

62

63

64

65

66

67

68

69

70

71

72

73

74

75

76

77

78

79

80

81

82

through which to discover novel disease-associated genes<sup>10</sup>. It has proven to be a highly powerful tool in the research and diagnosis context of male infertility 11,12. In addition, validation of newly-identified variants through functional experiments has greatly benefited from the ability to generate mouse knock-out models using CRISPR technology<sup>13</sup> and the use of novel model organisms like Trypanosoma brucei to study specific phenotypes, such as multiple morphological abnormalities of the [sperm] flagella (MMAF) syndrome <sup>14-16</sup>. These developments have resulted in a diagnostic yield, based on known genetic causes, explaining about 50% of cases of rare qualitative sperm defects like globozoospermia, acephalic, or MMAF syndromes <sup>17-18</sup>. In contrast, the diagnostic yield for quantitative sperm abnormalities such as oligozoospermia or azoospermia remains below 20%, even though these are the most common forms of male infertility<sup>8,12,19</sup>. To improve these low diagnostic yields, international consortia have been created to attempt to identify very low-frequency variants (https://gemini.conradlab.org/ and https://www.imigc.org/). In addition, several groups have started to assemble cohorts of patient-parent trios, aiming to identify de novo mutations causing male infertility as well as providing insight into dominant maternal inheritance 11,20,21. Phenotypic heterogeneity and apparent incomplete penetrance were observed for some genetic alterations involved in male infertility<sup>22-24</sup>. These observations are difficult to reconcile with a model of Mendelian inheritance. We thus raised the possibility that the low diagnostic yield is partly due to the complex etiology of infertility, and hypothesized that some of the unsolved cases are due to oligogenic events, i.e., accumulation of several rare hypomorphic variants in distinct, functionally connected genes, and in particular to oligogenic heterozygosity. The molecular basis of oligogenicity is poorly understood. The main hypotheses are that two or more mutant proteins may act at different levels in the same intracellular pathway and could quantitatively contribute to its progressive dysfunction. When a critical threshold is reached, the disease phenotype would emerge. Alternatively, the mutant

nonfunctional proteins produced may be part of the same multiprotein complex, and the presence of numerous pathogenic variants would increase the chance of the complex becoming compromised – leading to a progressive collapse of its cellular function<sup>25</sup>.

Here, we addressed the oligogenic heterozygosity hypothesis in male infertility using four specially-generated MMAF knock-out (KO) mouse models with autosomal recessive inheritance 14,26. Following extensive cross-breeding of our KO mouse lines, we produced lines harboring between one and four heterozygous truncating mutations. We assessed and compared fertility for these lines, analyzing both quantitative and qualitative sperm parameters, and performed a fine analysis of sperm nuclear morphology for all strains. Using this strategy, we were able to describe new genetic inheritance of sperm deficiencies.

## RESULTS

Selection and characterization of individual MMAF mouse lines. To generate mice carrying up to four heterozygous truncating mutations, we first selected four lines carrying mutations in genes inducing a MMAF phenotype, namely *Cfap43*, *Cfap44*, *Armc2*, and *Ccdc146*. Three of these lines were already available and previously reported by our laboratory: a strain with a 4-bp deletion in exon 21 (delAAGG) for *Cfap43*<sup>14</sup>, a strain with a 7-bp insertion in exon 3 (InsTCAGATA) for *Cfap44*<sup>14</sup>, and a strain with a one-nucleotide duplication in exon 4 (DupT) for *Armc2*<sup>26</sup>, inducing a translational frameshift that leads to the production of a truncated protein. We generated the fourth strain using CRISPR-Cas9 technology as described in the material and methods section, inducing a 4-bp deletion in exon 2 (delTTCG) of the *Ccdc146* gene (Supplementary Figure 1). A study describing how this mutation in the *Ccdc146* gene affects spermatogenesis is currently under review elsewhere (for the reviewers only, we provide the complete phenotype for the Ccdc146 KO mouse strain, demonstrating its role in MMAF syndrome in mice).

108

109

110

111

112

113

114

115

116

117

118

119

120

121

122

123

124

125

126

127

128

129

130

We first confirmed the MMAF phenotypes for all four strains. Sperm from all homozygous KO male mice displayed more than 95% morphological abnormalities of the flagellum including coiled, bent, irregular, short or/and absent flagella (Figures 1-4). We then analyzed sperm morphology (head and flagellum) in heterozygous animals by optical microscopy. The four strains fell into two categories. For the two strains targeting Cfap43 and Cfap44, Cfap43<sup>+/-</sup>, or Cfap44<sup>+/-</sup> heterozygous males had slightly higher rates of abnormalities than wild-type mice (Figure 1B and 2B; Cfap43: t=-2.79, df=6.13, p-value=0.03; Cfap44: t=-8.80, df=6.14, p-value=0.0001). These results were in accordance with previous observations<sup>14</sup>. In contrast, for strains harboring heterozygous mutations in Armc2 and Ccdc146, no significant differences were observed with respect to wild-type males (Figure 3B and 4B). Because head morphology defects may be subtle and difficult to detect by visual observation, we applied a newly-developed method, involving the use of Nuclear Morphology Analysis Software (NMAS)<sup>27</sup>. The method is described in detail in the material and methods section. The nuclear morphologies of sperm from each genotype (WT, heterozygotes, and homozygotes) were characterized. For all corresponding wild-type strains, shape modeling gave extremely similar consensus and angle profiles for nuclei, highlighting the common genetic background of the KO animals (Supplementary figure 2). For heterozygous Cfap43<sup>+/-</sup>, Cfap44<sup>+/-</sup>, and Ccdc146<sup>+/-</sup> individuals, the angle profiles were very similar to WT profiles (Figure 1C, 2C, and 4C). In contrast,  $Armc2^{+/-}$  individuals showed a slightly modified angle profile compared to the WT profile, due to a narrower caudal base inducing a more pronounced caudal bulge and a reduced dorsal angle (Figure 3C). When the profiles for all heterozygous males were compared, a very similar nuclear morphology with nearly identical angle and variability profiles was found, apart from for Armc2<sup>+/-</sup>, which had slightly more variability than the other lines despite a similar angle profile (Supplementary Figure 3).

132

133

134

135

136

137

138

139

140

141

142

143

144

145

146

147

148

149

150

151

152

153

154

155

We also compared these profiles with those of the corresponding KO mice, which displayed very unique and specific patterns (Figure 1C, 2C, 3C, 4C). Briefly, Cfap43<sup>-/-</sup> and Cfap44<sup>-/-</sup> angle profiles both displayed a flattening from the ventral angle to the dorsal angle leading to their characteristic "pepper" shape. The lines for both profiles merged over the majority of regions such as the under-hook concavity and the acrosomal curve, and showed intermediate impairment, greater than that observed in the Armc2<sup>-/-</sup> line and less than that observed in the Ccdc146<sup>-/-</sup> line. The angle profile for Armc2<sup>-/-</sup> individuals was similar to that of wild-type individuals at the tip, dorsal angle, and acrosomal curve, as these regions do not appear to be affected by the mutation. Under-hook concavity, ventral angle, and tail socket regions were slightly affected, although less than in other lineages. In contrast to the other lineages, the caudal base was markedly shortened, with a significant flattening observed. For the Ccdc146<sup>-/-</sup> line, with the exception of the ventral-vertical region, which was unaffected in any lineage, all regions of the angle profile were strongly impacted. The dorsal angle was completely absorbed into the acrosomal curve, and the under-hook concavity, ventral angle and caudal bulge regions were flattened. The tail socket region even displayed an inverted angular profile compared to the other lineages. Overall, the profile of Ccdc146<sup>-/-</sup> showed considerable variability, and complete remodeling of the angle profile with, among other changes, total inversion of the curve at position 330-400, corresponding to complete disappearance of the tail socket. Comparison of the profiles for KO sperm (Supplementary Figure 4) showed that Cfap43<sup>-/-</sup> and Cfap44<sup>-/-</sup> individuals displayed similar alterations (general enlargement of the head, rounding of the base at the expense of the flagellum insertion, etc.) resulting in close consensus; the other two lines were quite distinct. Whereas it was the most affected heterozygous line, Armc2<sup>-/-</sup> mice displayed the mildest alterations to nuclear morphology and variability of the four lines. KO animals nonetheless retained specific patterns, including modification of the hook curve and a specific slope of the base profile. Finally, Ccdc146<sup>-/-</sup>

157

158

159

160

161

162

163

164

165

166

167

168

169

170

171

172

173

174

175

176

177

178

179

individuals displayed extremely severe alterations, with almost all of their nuclei presenting a triangular shape (Figure 4DE). These results demonstrate for the first time that absence of MMAF genes not only affects sperm flagellum biogenesis but also has a dramatic impact on sperm head morphology. From these extensively characterized lines, we then proceeded to generate individuals harboring multiple mutations. **Impact of accumulation of heterozygous mutations.** All individuals harboring between one and four heterozygous truncating mutations were generated by standard cross-breeding of the four lines. A considerable number of generations were produced over several years. Due to time and financial constraints, only one combination of multiple heterozygous lines was created and analyzed. Double heterozygotes were obtained by crossing Cfap43 and Cfap44 KO mouse lines. Triple heterozygous animals were mutated for Cfap43, Cfap44, and Armc2; and the quadruple heterozygous line also had the *Ccdc146* mutation (Figure 5). The accumulation of heterozygous mutations on the four selected genes involved in MMAF syndromes induced qualitative spermatogenesis defects, with increased numbers of morphological anomalies (Figure 5A), in particular defects of the head (Figure 5B). In contrast, flagellar anomalies were not amplified as the number of mutated genes increased (Figure 5C). Nevertheless, accumulation of mutations had a negative impact on sperm motility parameters. Although the overall percentage of motile cells decreased only slowly with increasing numbers of mutations (Figure 5D), the quality of sperm movement was strongly affected (Figure 5E-5F). Thus, for sperm bearing two mutations, the average sperm velocity and straight-line velocity were halved compared to control individuals, and the decreasing trend continued as mutations accumulated. It is worth noting that adding Ccdc146 and Armc2 heterozygous mutations aggravated the phenotype, even though the heterozygous

181

182

183

184

185

186

187

188

189

190

191

192

193

194

195

196

197

198

199

200

201

202

203

mutations alone had no impact on the sperm phenotype observed by optical microscopy (Figure 3B and 4B). From the crosses performed to generate multi-heterozygous animals, other combinations of heterozygous mutations were obtained. The sperm parameters of the corresponding animals were also phenotyped. Interestingly, rates of morphological defect (Figure 6A-C, red dots) and motility parameters (Figure 6D-F, red dots) were very similar whatever the gene combinations. Taken together, these results show that it is not the specific combination of heterozygous mutations that leads to altered sperm morphology and sperm motility parameters, but rather their accumulation. Despite a marked alteration of spermatocytograms, accumulation of mutations did not have a significant effect on quantitative spermatogenesis defects. For example, sperm production – represented by testis weight and sperm concentration – and overall fertility of the animals – based on the number of pups per litter and interval between litters – were not affected, whatever the combination and number of mutations (Figure 7). As for mouse lines bearing single mutations, we then used NMAS to help characterize head anomalies in multi-heterozygote mutated lines. Our results indicated a striking progressive deterioration in sperm head morphology as mutations accumulated (Figure 8). Each additional mutation progressively and significantly increased the variability and severity of the morphological defects observed in the nucleus, negatively influencing angle and consensus profiles. This negative effect was cumulative, and if a threshold or plateau effect exists, it was not reached upon accumulation of four mutations. To extend our analysis, we then used the software to analyze sperm sub-populations by performing unbiased nuclear morphology categorization. Clustering based on angle profiles revealed a total of ten sub-groups of nuclei shape, which matched with the usual shapes of normal and abnormal mouse sperm, defined more than 30 years ago<sup>28</sup>. Mutation-accumulation progressively increased the frequency of all abnormal shapes and decreased the frequency of normal forms. The most unstructured forms were associated with the highest number of mutations (Supplementary figure 5).

## **DISCUSSION**

204

205

206

207

208

209

210

211

212

213

214

215

216

217

218

219

220

221

222

223

224

225

226

227

The aim of this study was to determine whether the accumulation of several rare heterozygous variants in functionally connected genes affected fertility and sperm parameters in mice. Our results clearly demonstrated that spermatogenesis failure can arise from oligogenic heterozygosity in mice. Males bearing increased numbers of heterozygote mutations in genes involved in MMAF syndrome exhibited altered spermatocytogram, with a greater proportion of abnormal sperm and decreased sperm motility. However, these alterations had no effect on male fertility, suggesting that we had not reached the threshold leading to the complete collapse of the male reproductive function. This concept of threshold is strongly associated with oligogenicity. It is defined by the number of mutations within the same multiprotein complex or intracellular pathway beyond which a disease phenotype will be observed<sup>29</sup>. In this study, we induced mutations in four genes coding for proteins participating in flagella formation and function. Although we did observe a negative cumulative burden, we did not reach the complex or system threshold that would lead to the emergence of a dichotomous severe infertility phenotype. Nevertheless, mice have particularly efficient sperm production and their male and female reproductive functions are generally robust. A similar mutational burden in humans - known to have the highest number of sperm defect among primates<sup>30</sup> could, however, be sufficient to reach the threshold for fertility collapse. It is worth noting that the probability of accumulating this type of heterozygous mutations in testis is considerable, because i) thousands of genes are necessary to achieve spermatogenesis<sup>9</sup>, ii)

229

230

231

232

233

234

235

236

237

238

239

240

241

242

243

244

245

246

247

248

249

250

251

252

expression of most spermatogenesis-associated genes is restricted to or strongly enriched in the testis<sup>31</sup>, and consequently iii) the risk of life-threatening impact of mutations is limited. Moreover, mutant gene products retaining some residual function could be influenced by additional systemic perturbation (see review in <sup>32</sup>) that would lead to system collapse. For instance, environmental factors commonly responsible for milder alterations spermatogenesis could play an important role by severely aggravating the genetic burden on the system. This type of multi-factorial input could explain the phenotypic continuum observed in patients with idiopathic infertility. In this article, we showed that the haplo-insufficiency of several genes involved in flagellum biogenesis and associated with MMAF syndrome leads to head defects. The impact of the accumulation of mutations in the heterozygous state on the morphology of the head is in agreement with our results (presented above and previously published<sup>14</sup>) showing that the complete lack of these genes in KO males also strongly alters head patterning. Unexpectedly, accumulation of heterozygous mutations led to marked head defects without obvious morphological defects of the flagellum. This observation suggests that head shape is more prone to collapse than flagellum biogenesis. For the first time, we were able to objectively document these defects using NMAS. This original method allows objective comparison of the impact of mutations on sperm head morphology, and represents a breakthrough in sperm morphology assessment in a pathological context. The NMAS method was also used to analyze head morphology in sperm produced by KO males. We found that sperm from Cfap43<sup>-/-</sup> and Cfap44<sup>-/-</sup> mice predominantly displayed a "pepper" shape – characterized by a strong broadening of the base and a reduced size of the flagellum insertion notch. Armc2<sup>-/-</sup> sperm show moderate enlargement extending along the entire length of the head, including the hook, and an increase in circularity resulting in a more rounded appearance. Ccdc146<sup>-/-</sup> sperm presented a total disorganization of the base with complete erasure of the flagellum

254

255

256

257

258

259

260

261

262

263

264

265

266

267

268

269

270

271

272

273

274

275

276

277

insertion notch, and an overall decrease in size, resulting in heads with a triangular aspect characteristic of the "claw" shape. The reasons why mutations in flagellar proteins have such a strong impact on head morphology remain unclear, however the effect on sperm head shape was gene-dependent, with a milder effect observed for Armc2 and a stronger effect observed for Cfap43, Cfap44, and Ccd146. This result was notable as the flagellum phenotype of Armc2 is as severe as that observed with mutation of the other genes. Consequently, sperm head defects are not due to failed flagellum biogenesis. Rather, we hypothesize that some proteins contribute not only to flagellum biogenesis, but also to various cytoskeletal components including the manchette, a key organelle in sperm head shaping<sup>33</sup>. For instance, a recent report showed that lack of Cfap43 affects intra-manchette transport<sup>34</sup>. Thus, compared to the other proteins, Armc2 may be less involved in functions other than flagellum biogenesis. Therefore, we recommend that head morphology should not be overlooked when studying MMAF syndromes, despite an obvious focus on flagellum anomalies. Among the proteins encoded by previously identified MMAF genes, some belong to complexes involved in intraflagellar transport<sup>35-37</sup>, protein degradation<sup>38</sup> or unknown processes<sup>26,39</sup> that could affect head formation, and subsequently sperm DNA. As there is a strong relationship between cytoskeletal and chromosomal effects, the question of the potential impact of the accumulation of mutations on sperm chromatin organization arises. Another interesting question would be to investigate whether the damaged heads correspond to those carrying the mutated alleles. Future studies will be eagerly awaited to elucidate the molecular basis of oligogenicity in male infertility. Moreover, as descriptions of animal reproductive phenotypes are becoming increasingly sophisticated and standardized<sup>40</sup>, emerging tools such as the software used in this study to analyze nuclear morphology should be used to extensively study reproductive phenotypes, including studies of MMAF syndromes, to accurately document head defects.

279

280

281

282

283

284

285

286

287

288

289

290

291

292

293

294

295

296

297

298

299

300

301

302

Despite a strong focus on sperm head defects, we also showed that sperm motility was altered in the presence of  $\geq 2$  heterozygote mutations. Thus, the function of the flagellum is affected, and an absence of morphological defects should therefore not be considered synonymous with absence of functional defects. More importantly, this result strongly suggests for the first time that idiopathic human asthenozoospermia may be due to an accumulation of heterozygous mutations in genes known to be involved in flagellum biogenesis. To date, the inheritance pattern of isolated male infertility was only known to be Mendelian – i.e., based on a single locus - and the possibility of oligogenic inheritance had not been explored. In contrast, an oligogenic etiology for female infertility has been proposed to be associated with primary ovarian insufficiency (POI) by several groups, in particular due to the identification of heterozygous mutations in several genes associated with POI<sup>41</sup>. Oligogenic inheritance has also previously been suggested in another reproductive disorder: congenital hypogonadotropic hypogonadism<sup>42</sup>, as well as in several non-reproductive disorders<sup>43</sup>. Our results demonstrate that oligogenic inheritance may be linked to both male and female human infertility, and should therefore also be accurately measured when investigating male infertility. In conclusion, in this article, we report the first evidence of oligogenic inheritance in altered spermatogenesis, leading to teratoasthenozoospermia. This mode of inheritance is crucial as oligogenic events could be behind the difficulties encountered by a significant proportion of infertile couples, for whom the current diagnosis is the somewhat unsatisfactory "unexplained" or "idiopathic" infertility. Our study was conducted in a context of teratozoospermia, a qualitative disorder of spermatogenesis. It paves the way for further studies on other male infertility disorders, including quantitative disorders, such as oligozoospermia or azoospermia for which the diagnostic yield remains very low. In particular, international consortia will benefit from this new understanding of the genetic

factors influencing spermatogenesis by incorporating it into their scientific strategies. Current genetic tests to explore male infertility focus primarily on identifying low-frequency fullypenetrant monogenic defects, which are usually autosomal recessive and linked to the most severe cases of male infertility. However, investigation of oligogenic inheritance in the huge cohorts available should provide an estimate of the frequency of such events. These investigations could potentially identify new candidate genes involved in male infertility. The discovery presented here is of major medical interest, and has implications for both clinical genetics and infertility management. First, the continuous and exponential characterization of new genes involved in infertility over the last decade offers the hope that, in the near future, an almost exhaustive list of genes and mutations involved in human infertility will be available. The identification of and screening for all known mutant alleles linked to male infertility at the heterozygous level should improve the diagnostic yield. Second, the discovery of multiple mutated genes will allow clinicians to provide more accurate genetic counselling to patients, and better guide them in their infertility journey. To improve patient management, future studies should look at potential correlations between patients' mutational burden and their intracytoplasmic sperm injection (ICSI) success, pregnancies achieved, and live birth rates. It will also be essential to assess the impact of mutational load on parameters known to influence these outcomes.

## **METHODS**

## **Animals**

303

304

305

306

307

308

309

310

311

312

313

314

315

316

317

318

319

320

321

322

323

324

325

326

Generation of *Cfap43* and *Cfap44* KO mice is described in Coutton et al. (2018)<sup>14</sup>, generation of *Armc2* KO mice is described in Coutton et al. (2019)<sup>26</sup>. CRISPR/Cas9 gene editing was used to produce *Ccdc146* KO mice (ENSMUST00000115245). To maximize the chances of producing deleterious mutations, two gRNAs located in two distinct coding exons positioned

328

329

330

331

332

333

334

335

336

337

338

339

340

341

342

343

344

345

346

347

348

349

350

351

at the beginning of the targeted gene were used. For each gene, the two gRNAs (5'-CCT ACA GTT AAC ATT CGG G-3' and 5'-GGG AGT ACA ATA TTC AGT AC-3') targeting exons 2 and 4, respectively, were inserted into two distinct plasmids also containing the Cas9 sequence. The Cas9 gene was driven by a CMV promoter and the gRNA and its RNA scaffold by a U6 promoter. Full plasmids (pSpCas9 BB-2A-GFP (PX458)) containing the specific sgRNA were ordered from Genescript (https://www.genscript.com/crispr-cas9protein-crRNA.html). Both plasmids were co-injected into the zygotes' pronuclei at a concentration of 2.5 ng/ml. It should be noted that the plasmids were injected as delivered by the supplier, thus avoiding the need to perform in vitro production and purification of Cas9 proteins and sgRNA. Several mutated animals were obtained with different insertions/deletions spanning a few nucleotides. All of the mutations obtained induced a translational frameshift expected to lead to complete absence of the protein or production of a truncated protein. The reproductive phenotype of two mutated lines was analyzed; homozygous males were infertile and displayed the same MMAF phenotype. For this study, a strain with a 4-bp deletion in exon 2 was used (c.164\_167delTTCG). For each KO strain, mice were maintained in the heterozygous state, and males and females were crossed to produce animals for subsequent generations. Heterozygous and homozygous animals were selected following PCR screening, the primers used for each strain are indicated in Supplementary Table 5. To produce multi-heterozygous animals, homozygous females were crossed with heterozygous males. All animal procedures were conducted according to a protocol approved by the local Ethics Committee (ComEth Grenoble No. 318), by the French government (ministry agreement number #7128 UHTA-U1209-CA), and by the Direction Générale de la Santé (DGS) for the State of Geneva. Guide RNA, TracrRNA, ssDNA, and Cas9 were purchased from Integrated DNA Technologies. Pronuclear injection and embryo transfer were performed by the

Transgenic Core facility at the Faculty of Medicine, University of Geneva. All genotypes

were obtained by conventional interbreeding.

## Reproductive phenotyping

352

353

354

355

356

357

358

359

360

361

362

363

364

365

366

367

368

369

370

371

372

373

374

375

All adult male mice used were between 10 and 12 weeks old. After sacrifice by cervical dislocation, the testes were isolated and weighed, and sperm from caudae epididymides were allowed to swim for 10 min at 37 °C in 1 ml of M2 medium (Sigma-Aldrich, L'Isle d'Abeau, France). The sperm concentration was measured and adjusted before CASA analysis. An aliquot of sperm suspension was immediately placed in a 100-µm deep analysis chamber (Leja Products B.V., Nieuw-Vennep, the Netherlands), and sperm motility parameters were measured at 37 °C using a sperm analyzer (Hamilton Thorn Research, Beverley, MA, USA). The settings used for analysis were: acquisition rate: 60 Hz; number of frames: 45; minimum contrast: 50; minimum cell size: 5; low static-size gate: 0.3; high static-size gate: 1.95; low static-intensity gate: 0.5; high static-intensity gate: 1.3; minimum elongation gate: 0; maximum elongation gate: 87; magnification factor: 0.7. Motile sperm were defined by an average path velocity (VAP) > 1, and progressive sperm motility was defined by VAP > 30 and average path straightness > 70. A minimum of 200 motile spermatozoa were analyzed in each assay. Remaining sperm was rinsed with PBS-1X, centrifuged for 5 min at 500 g, spread on slides and allowed to dry at room temperature. Samples were then fixed in Ether/Ethanol 1:1 for Harris-Schorr staining (to assess overall morphology) or in 4% paraformaldehyde for DAPI staining (to assess nuclear morphology). Morphology was assessed on a Nikon Eclipse 80i microscope equipped with a Nikon DS-Ri1 camera with NIS-ElementsD (version 3.1.) software. At least 200 spermatozoa were counted per slide at a magnification of  $\times 1000$ .

## Analysis of nuclear morphology

Nuclear morphology was precisely evaluated by NMAS (version 1.19.2), according to the analysis method described in Skinner et al. 27. The software processed images of DAPI-stained nuclei captured with a Zeiss Imager Z2 microscope, using a CoolCube 1 CCD camera, with a 100x/1.4 Zeiss objective and Neon software (MetaSystems, Altlussheim, Germany). Nucleus detection settings were Kuwahara kernel: 3, and flattening threshold: 100, for preprocessing; canny low threshold: 0.5, canny high threshold: 1.5, canny kernel radius: 3, canny kernel width: 16, gap closing radius: 5, to find objects; and min area: 1 000, max area: 10 000, min circ: 0.1, max circ: 0.9, for filtering. After acquisition of images of nuclei, landmarks were automatically identified using a modification of the Zahn-Roskies transform to generate an angle profile from the internal angles measured around the periphery of the nuclei. Angles were measured at every individual pixel around the original shape. This method combines data from every possible polygonal approximation into a single unified trace, from which landmark features can be detected (under-hook concavity, tail socket, caudal bulge and base, acrosomal curve, etc.). Angle profiles are presented as angle degrees according to the relative position of each pixel along the perimeter, and variability profiles use the interquartile range (IQR, difference between the third and first quartile) as a dispersion indicator to measure the variability of values obtained for each point. Sperm shape populations were then clustered using a hierarchical ward-distance method without reduction, based on angle profiles.

## STATISTICAL ANALYSIS

376

377

378

379

380

381

382

383

384

385

386

387

388

389

390

391

392

393

394

395

396

397

398

The statistics relating to nuclear morphology presented in Figure 8 and Supplementary Figure 4, were automatically calculated by the Nuclear Morphology Analysis Software. This analysis relied on a Mann-Whitney U test with Bonferroni multiple testing correction. p-values were considered significant when inferior to 0.05.

- All other data were treated with R software (version 3.5.2). Histograms show mean  $\pm$  standard
- 400 deviation, and statistical significance of differences was assessed by applying an unpaired t-
- 401 test. Statistical tests with two-tailed p-values  $\leq 0.05$  were considered significant.

## DATA AVAILABILITY

- 403 All data that support the findings of this study are available from the corresponding authors
- 404 upon reasonable request.

402

405

## REFERENCES

- 1. Mascarenhas, M., Flaxman, S., Boerma, T., Vanderpoel, S. & Stevens, G. National,
- 407 regional, and global trends in infertility prevalence since 1990: A systematic analysis of 277
- 408 health surveys. *PLoS Medicine* 9, e1001356 (2012).
- 409 2. Boivin, J., Bunting, L., Collins, J. & Nygren, K. International estimates of infertility
- 410 prevalence and treatment-seeking: potential need and demand for infertility medical care.
- 411 *Human Reproduction* 22, 1506-1512 (2007).
- 3. Sun, H. et al. Global, regional, and national prevalence and disability-adjusted life-years for
- 413 infertility in 195 countries and territories, 1990–2017: results from a global burden of disease
- 414 study, 2017. Aging 11, 10952-10991 (2019).
- 4. Datta, J. et al. Prevalence of infertility and help seeking among 15 000 women and men.
- 416 *Human Reproduction* 31, 2108-2118 (2016).
- 5. Faddy, M., Gosden, M. & Gosden, R. A demographic projection of the contribution of
- 418 assisted reproductive technologies to world population growth. Reproductive BioMedicine
- 419 *Online* 36, 455-458 (2018).
- 420 6. Fauser, B. Towards the global coverage of a unified registry of IVF outcomes.
- 421 Reproductive BioMedicine Online 38, 133-137 (2019).

- 422 7. Sadeghi, M. Unexplained infertility, the controversial matter in management of infertile
- 423 couples. *Journal of reproduction & infertility* 16, 1-2 (2021).
- 8. Krausz, C. Male infertility: Pathogenesis and clinical diagnosis. Best Practice & Research
- 425 Clinical Endocrinology & Metabolism 25, 271-285 (2011).
- 426 9. Jan, S. et al. Unraveling transcriptome dynamics in human spermatogenesis. *Development*
- 427 (2017). doi:10.1242/dev.152413
- 428 10. Fernandez-Marmiesse, A., Gouveia, S. & Couce, M. NGS Technologies as a Turning
- Point in Rare Disease Research, Diagnosis and Treatment. Current Medicinal Chemistry 25,
- 430 404-432 (2018).
- 431 11. Xavier, M., Salas-Huetos, A., Oud, M., Aston, K. & Veltman, J. Disease gene discovery
- in male infertility: past, present and future. *Human Genetics* 140, 7-19 (2020).
- 433 12. Krausz, C. & Riera-Escamilla, A. Genetics of male infertility. *Nature Reviews Urology*
- 434 15, 369-384 (2018).
- 13. Kherraf, Z. et al. Creation of knock out and knock in mice by CRISPR/Cas9 to validate
- candidate genes for human male infertility, interest, difficulties and feasibility. *Molecular and*
- 437 *Cellular Endocrinology* 468, 70-80 (2018).
- 438 14. Coutton, C. et al. Mutations in CFAP43 and CFAP44 cause male infertility and flagellum
- defects in Trypanosoma and human. *Nature Communications* 9, (2018).
- 440 15. Lorès, P. et al. Mutations in TTC29, Encoding an Evolutionarily Conserved Axonemal
- 441 Protein, Result in Asthenozoospermia and Male Infertility. The American Journal of Human
- 442 Genetics 105, 1148-1167 (2019).
- 443 16. Martinez, G. et al. Biallelic variants in MAATS1 encoding CFAP91, a calmodulin-
- associated and spoke-associated complex protein, cause severe astheno-teratozoospermia and
- male infertility. *Journal of Medical Genetics* **57**, 708–716 (2020).

- 446 17. Beurois, J. et al. Genetics of teratozoospermia: Back to the head. Best Practice &
- 447 Research Clinical Endocrinology & Metabolism **34**, 101473 (2020).
- 18. Touré, A. et al. The genetic architecture of morphological abnormalities of the sperm tail.
- 449 *Human Genetics* **140,** 21–42 (2020).
- 450 19. Tüttelmann, F., Ruckert, C. & Röpke, A. Disorders of spermatogenesis. medizinische
- 451 *genetik* **30,** 12–20 (2018).
- 452 20. Veltman, J. A. & Brunner, H. G. De novo mutations in human genetic disease. *Nature*
- 453 *Reviews Genetics* **13,** 565–575 (2012).
- 454 21. McRae, J. et al. Prevalence and architecture of de novo mutations in developmental
- 455 disorders. *Nature* **542**, 433–438 (2017).
- 456 22. Vogt, P. H. AZF deletions and Y chromosomal haplogroups: history and update based on
- 457 sequence. *Human Reproduction Update* **11,** 319–336 (2005).
- 458 23. Röpke, A. et al. Comprehensive sequence analysis of the NR5A1 gene encoding
- 459 steroidogenic factor 1 in a large group of infertile males. European Journal of Human
- 460 *Genetics* **21**, 1012–1015 (2013).
- 461 24. Kherraf, Z. E. et al. SPINK 2 deficiency causes infertility by inducing sperm defects in
- heterozygotes and azoospermia in homozygotes. EMBO Molecular Medicine 9, 1132–1149
- 463 (2017).
- 464 25. Kousi, M. & Katsanis, N. Genetic Modifiers and Oligogenic Inheritance. *Cold Spring*
- 465 *Harbor Perspectives in Medicine* **5,** (2015).
- 466 26. Coutton, C. et al. Bi-allelic Mutations in ARMC2 Lead to Severe Astheno-
- 467 Teratozoospermia Due to Sperm Flagellum Malformations in Humans and Mice. The
- 468 *American Journal of Human Genetics* **104,** 331–340 (2019).
- 469 27. Skinner, B. M. et al. A high-throughput method for unbiased quantitation and
- categorization of nuclear morphology. *Biology of Reproduction* **100**, 1250–1260 (2019).

- 471 28. Krzanowska, H. Sperm head abnormalities in relation to the age and strain of mice.
- 472 Reproduction **62**, 385–392 (1981).
- 29. Dipple, K. M. & Mccabe, E. R. Phenotypes of Patients with "Simple" Mendelian
- Disorders Are Complex Traits: Thresholds, Modifiers, and Systems Dynamics. *The American*
- 475 *Journal of Human Genetics* **66,** 1729–1735 (2000).
- 476 30. Martinez, G. & Garcia, C. Sexual selection and sperm diversity in primates. *Molecular*
- *and Cellular Endocrinology* **518,** 110974 (2020).
- 478 31. Uhlén, M. et al. Transcriptomics resources of human tissues and organs. Molecular
- 479 *Systems Biology* **12**, 862 (2016).
- 480 32. Borght, M. V. & Wyns, C. Fertility and infertility: Definition and epidemiology. *Clinical*
- 481 *Biochemistry* **62**, 2–10 (2018).
- 482 33. Kierszenbaum, A. L. & Tres, L. L. The acrosome-acroplaxome-manchette complex and
- 483 the shaping of the spermatid head. Archives of Histology and Cytology 67, 271–284 (2004).
- 484 34. Yu, Y. et al. CFAP43-mediated intra-manchette transport is required for sperm head
- shaping and flagella formation. *Zygote* **29,** 75–81 (2020).
- 486 35. Liu, W. et al. Loss-of-function mutations in SPEF2 cause multiple morphological
- abnormalities of the sperm flagella (MMAF). Journal of Medical Genetics 56, 678-684
- 488 (2019).
- 36. Liu, W. et al. Homozygous loss-of-function mutations in FSIP2 cause male infertility with
- asthenoteratospermia. *Journal of Genetics and Genomics* **46**, 53–56 (2019).
- 491 37. Chung, M.-I. et al. Coordinated genomic control of ciliogenesis and cell movement by
- 492 RFX2. *eLife* **3**, (2014).
- 38. Shen, Y. et al. Loss-of-function mutations in QRICH2 cause male infertility with multiple
- 494 morphological abnormalities of the sperm flagella. *Nature Communications* **10**, (2019).

- 495 39. Lorès, P. et al. Homozygous missense mutation L673P in adenylate kinase 7 (AK7) leads
- 496 to primary male infertility and multiple morphological anomalies of the flagella but not to
- 497 primary ciliary dyskinesia. *Human Molecular Genetics* **27**, 1196–1211 (2018).
- 498 40. Houston, B. J., Conrad, D. F. & O'Bryan, M. K. A framework for high-resolution
- 499 phenotyping of candidate male infertility mutants: from human to mouse. *Human Genetics*
- 500 **140,** 155–182 (2020).
- 501 41. Patiño, L. C. et al. New mutations in non-syndromic primary ovarian insufficiency
- patients identified via whole-exome sequencing. *Human Reproduction* **32,** 1512–1520 (2017).
- 503 42. Pitteloud, N. et al. Digenic mutations account for variable phenotypes in idiopathic
- 504 hypogonadotropic hypogonadism. *Journal of Clinical Investigation* **117**, 457–463 (2007).
- 43. Li, L., Bainbridge, M. N., Tan, Y., Willerson, J. T. & Marian, A. J. A Potential Oligogenic
- Etiology of Hypertrophic Cardiomyopathy. *Circulation Research* **120**, 1084–1090 (2017).

## **ACKNOWLEDGEMENTS**

507

508

514

515

- 509 This work was supported in part by the French national research agency grants FLAGEL-
- 510 OME: ANR-19-CE17-0014 and OLIGO-SPERM: ANR-21-CE17-00XX. We would like to
- sincerely thank Roxane DOMINGUEZ and Aurélien SIMON for their assistance with the
- 512 software and IT solutions. We are also grateful to Charlotte GUYOT and Marlène
- 513 GANDULA for technical assistance.

## **AUTHOR CONTRIBUTIONS**

- 516 G.M., C.C., P.F.R., and C.A. analyzed the data and wrote the manuscript; C.Ca., M.B., Z.-
- 517 E.K., Y.N., and S.N. performed genetic work; G.M., C.L., E.L., M.D., G.C., C.V., J.M., J.-
- P.H., Y.N., S.N., and J.E. performed mouse work; G.M., C.C., P.F.R., and C.A. designed the

study, supervised all laboratory work, had full access to all of the data from the study and take responsibility for the integrity of the data and its accuracy. All authors contributed to the report.

## **COMPETING INTERESTS**

The authors declare no competing financial interests.

## MATERIALS & CORRESPONDANCE

- Requests should be addressed to G.M. (gmartinez@chu-grenoble.fr) and C.A.
- 528 (christophe.arnoult@univ-grenoble-alpes.fr).

## **FIGURES**

Figure 1. Sperm morphology analysis for the *Cfap43* mouse strain. A. Graphical representation of the location and numbering of the regions of interest presented in the lineage profiles (from  $^{27}$ ) with: 1-tip; 2-under-hook concavity; 3-vertical; 4-ventral angle; 5-tail socket; 6-caudal bulge; 7-caudal base; 8-dorsal angle; 9-11-acrosomal curve. **B.** Histogram showing proportions of morphological anomalies (mean  $\pm$  SD) for each *Cfap43* genotype. Statistical significance was assessed by applying an unpaired *t*-test; *p*-values are indicated. **C.** Angle profiles (top) and variability profiles (bottom) from *Cfap43*<sup>+/+</sup> (blue), *Cfap43*<sup>+/-</sup> (yellow), and *Cfap43*<sup>-/-</sup> (green) mice. The x axis represents an index of the percentage of the total perimeter as measured counterclockwise from the apex of the sperm hook. The y axis corresponding to the angle profile represents the interior angle measured across a sliding

542

543

544

545

546

547

548

549

550

551

552

553

554

555

556

557

558

559

560

561

562

563

564

565

window centered on each index location. The y axis corresponding to the variability profile represents the Interquartile Range (IQR) value (the difference between the 75th and 25th percentiles). Specific regions of the nuclei are mapped on both axes as indicated in A. D. Consensus nuclear outlines for each genotype alongside a merged consensus nucleus (blue= $Cfap43^{+/+}$ , yellow=  $Cfap43^{+/-}$ , green=  $Cfap43^{-/-}$ ). The numbers assigned to each consensus outline correspond to the number of nuclei processed per condition. E. Optical microscopy analysis showing a representative MMAF phenotype for Cfap43 KO mice (scale bar, 10 µM). Figure 2. Sperm morphology analysis for the Cfap44 mouse strain. A. Graphical representation of the location and numbering of the regions of interest presented in the lineage profiles (from <sup>27</sup>) with: 1-tip; 2-under-hook concavity; 3-vertical; 4-ventral angle; 5-tail socket; 6-caudal bulge; 7-caudal base; 8-dorsal angle; 9-11-acrosomal curve. **B.** Histogram showing proportions of morphological anomalies (mean  $\pm$  SD) for each Cfap44 genotype. Statistical significance was assessed by applying an unpaired t-test; p-values are indicated. C. Angle profiles (top) and variability profiles (bottom) for Cfap44<sup>+/+</sup> (blue), Cfap44<sup>+/-</sup> (yellow), and Cfap44<sup>-/-</sup> (green) mice. The x axis represents an index of the percentage of the total perimeter, as measured counterclockwise from the apex of the sperm hook. The y axis corresponding to the angle profile is the interior angle measured across a sliding window centered on each index location. The y axis corresponding to the variability profile represents the Interquartile Range (IQR) value (the difference between the 75<sup>th</sup> and 25<sup>th</sup> percentiles). Specific regions of the nuclei are mapped on both axes as indicated in Fig. 1A. **D.** Consensus nuclear outlines for each genotype alongside a merged consensus nucleus (blue= $Cfap44^{+/+}$ , vellow= Cfap44<sup>+/-</sup>, green= Cfap44<sup>-/-</sup>). The numbers assigned to each consensus outline correspond to the number of nuclei processed per condition. E. Optical microscopy analysis showing a representative MMAF phenotype for *Cfap44* KO mice (scale bar, 10 µM).

567

568

569

570

571

572

573

574

575

576

577

578

579

580

581

582

583

584

585

586

587

588

589

590

Figure 3. Sperm morphology analysis for the Armc2 mouse strain. A. Graphical representation of the location and numbering of the regions of interest presented in the lineage profiles (from <sup>27</sup>) with: 1-tip; 2-under-hook concavity; 3-vertical; 4-ventral angle; 5-tail socket; 6-caudal bulge; 7-caudal base; 8-dorsal angle; 9-11-acrosomal curve. B. Histogram showing proportions of morphological anomalies (mean  $\pm$  SD) for each Armc2 genotype. Statistical significance was assessed by applying an unpaired t-test; p-values are indicated. C. Angle profiles (top) and variability profiles (bottom) for  $Armc2^{+/+}$  (blue),  $Armc2^{+/-}$  (yellow), and Armc2<sup>-/-</sup> (green) mice. The x axis represents an index of the percentage of the total perimeter, as measured counterclockwise from the apex of the sperm hook. The y axis corresponding to the angle profile represents the interior angle measured across a sliding window centered on each index location. The y axis corresponding to the variability profile represents the Interquartile Range (IQR) value (the difference between the 75th and 25th percentiles). Specific regions of the nuclei are mapped on both axes as indicated in Fig. 1A. **D.** Consensus nuclear outlines for each genotype alongside a merged consensus nucleus (blue= $Armc2^{+/+}$ , yellow= $Armc2^{+/-}$ , green= $Armc2^{-/-}$ ). The numbers assigned to each consensus outline correspond to the number of nuclei processed per condition. E. Optical microscopy analysis showing a representative MMAF phenotype for Cfap44 KO mice (scale bar, 10 µM). Figure 4. Sperm morphology analysis for the Ccdc146 mouse strain. A. Graphical representation of the location and numbering of the regions of interest presented in the lineage profiles (from <sup>27</sup>) with: 1-tip; 2-under-hook concavity; 3-vertical; 4-ventral angle; 5-tail socket; 6-caudal bulge; 7-caudal base; 8-dorsal angle; 9-11-acrosomal curve. **B.** Histogram showing proportions of morphological anomalies (mean  $\pm$  SD) for each *Ccdc146* genotype. Statistical significance was assessed by applying an unpaired t-test; p-values are indicated. C. Angle profiles (top) and variability profiles (bottom) for Ccdc146<sup>+/-</sup> (blue), Ccdc146<sup>+/-</sup> (yellow) and Ccdc146-/- (green) mice. The x axis represents an index of the percentage of the

592

593

594

595

596

597

598

599

600

601

602

603

604

605

606

607

608

609

610

611

612

613

614

615

total perimeter as measured counterclockwise from the apex of the sperm hook. The y axis corresponding to the angle profile is the interior angle measured across a sliding window centered on each index location. The y axis corresponding to the variability profile represents the Interquartile Range (IOR) (the difference between the 75<sup>th</sup> and 25<sup>th</sup> percentiles). Specific regions of the nuclei are mapped on both axes as indicated in Fig. 1A. D. Consensus nuclear outlines for each genotype alongside a merged consensus nucleus (blue=Ccdc146<sup>+/+</sup>, yellow=Ccdc146<sup>+/-</sup>, green=Ccdc146<sup>-/-</sup>). The numbers assigned to each consensus outline correspond to the number of nuclei processed per condition. E. Optical microscopy analysis showing a typical MMAF phenotype for *Ccdc146* KO mice (scale bar, 10 µM). Figure 5. Increasing the number of heterozygous mutated genes involved in the MMAF syndrome has a drastic effect on sperm morphology and motility. (A) Sperm morphological defects, (B) head anomalies, (C) flagellum defects, showing only slight impact. Increasing the number of heterozygous gene mutations had little effect on (D) Percentage of motile sperm, but considerably reduced sperm motility parameters including (E) average path velocity (VAP), and (F) curvilinear velocity (VCL). All data are presented simultaneously as box-plot and individual datapoints. Statistical significance was assessed using an unpaired ttest, and significantly different populations are identified by distinct letters. The corresponding statistical data can be found in Supplementary Tables 1-2. Figure 6. Very similar head morphology defects and decreased motility parameters, whatever the combination of mutated genes. Black dots correspond to the different combinations (2 = Cfap43 and Cfap44; 3 = Cfap43, Cfap44 and Armc2; 4 = Cfap43, Cfap44 and Armc2 and Ccdc146) of mutations presented in figure 5; red dots correspond to alternative combinations obtained with the same four genes. The range of (A) sperm morphological defects, (B) head anomalies, and (C) flagellum defects was similar for black and red dots. Likewise, (D) percentage of motile sperm, (E) average path velocity (VAP) and

617

618

619

620

621

622

623

624

625

626

627

628

629

630

631

632

633

634

635

636

637

638

639

640

(F) curvilinear velocity (VCL), showed similar ranges for black and red dots. All data are presented simultaneously as box-plot and individual datapoints. Statistical significance of differences between means calculated for all black and red dots were assessed by applying an unpaired t-test. Statistically different populations are identified by distinct letters. The corresponding statistical data can be found in Supplementary Tables 3-4. Figure 7. Increasing the number of mutated genes has little effect on overall fertility. (A) sperm production data (B) overall fertility of animals (measured as the interval between two litters and the number of pups per litter). All data are presented simultaneously as box-plot and individual datapoints. Statistical significance was assessed using an unpaired t-test, and significantly different populations are identified by distinct letters. The corresponding statistical data can be found in Supplementary Tables 5-6. Figure 8. Fine nuclear morphology analysis of multi-mutant mice with one to four heterozygous mutations. A. Consensus nuclear outlines for each strain alongside a merged consensus nucleus (blue=one mutation, yellow=two mutations, green=three mutations and pink=four mutations). The numbers assigned to each consensus outline correspond to the number of nuclei processed per condition. B. Angle profiles for each strain focusing (black boxes) on positions of specific interest. The x axis represents an index of the percentage of the total perimeter, as measured counterclockwise from the apex of the sperm hook. The y axis shows the interior angle measured across a sliding window centered on each index location. C. Variability profiles for each strain. The x axis is the same as for the angle profile, and the y axis represents the Interquartile Range (IQR) (the difference between the 75<sup>th</sup> and 25<sup>th</sup> percentiles). Specific regions of the nuclei are mapped on the profile and the graphical representation (from <sup>27</sup>), with: 1-tip; 2-under-hook concavity; 3-vertical; 4-ventral angle; 5-tail socket; 6-caudal bulge; 7-caudal base; 8-dorsal angle; 9-11-acrosomal curve. **D.** Violin plots of nuclear parameters for each strain. Statistical significance of differences between populations were assessed by the software, applying a Mann-Whitney U test; significantly different populations are identified by distinct letters.

## SUPPLEMENTARY INFORMATION

641

642

643

644

645

646

647

648

649

650

651

652

653

654

655

656

657

658

659

660

661

662

663

664

Supplementary Figure 1. Location of mutations and electropherograms from Sanger sequencing of mutated forms of murine Cfap43, Cfap44, Armc2, and Ccdc146 compared to their respective reference sequences. We confirmed a 4-bp deletion in Cfap43 exon 21 (delAAGG), a 7-bp insertion in Cfap44 exon 3 (InsTCAGATA), a 1-bp insertion (InsT) in Armc2 exon 4, and a 4-bp deletion in Ccdc146 exon 2 (delTTCG). Red arrows indicate the CRISPR/Cas9 targeting sequence, mutations are highlighted in yellow, and the gray boxes indicate the position of the protospacer-adjacent motif (PAM) sequences used during mutagenesis. **Supplementary Figure 2.** Comparison of fine nuclear morphology for wild-type animals produced from crosses of all strains studied. A. Consensus nuclear outlines for each strain alongside a merged consensus nucleus (blue=Cfap43, yellow=Cfap44, green=Armc2 and pink=Ccdc146). The numbers assigned to each consensus outline correspond to the number of nuclei processed per condition. **B.** Angle profiles for each strain focusing (black boxes) on positions of specific interest. The x axis represents an index of the percentage of the total perimeter, as measured counterclockwise from the apex of the sperm hook. The y axis shows the interior angle measured across a sliding window centered on each index location C. Variability profiles for each strain. The x axis is the same as for the angle profile, and the y axis represents the Interquartile Range (IQR) (the difference between the 75th and 25th percentiles). Specific regions of the nuclei are mapped on the profile and the graphical representation (from <sup>27</sup>), with: 1-tip; 2-under-hook concavity; 3-vertical; 4-ventral angle; 5-tail socket; 6-caudal bulge; 7-caudal base; 8-dorsal angle; 9-11-acrosomal curve.

666

667

668

669

670

671

672

673

674

675

676

677

678

679

680

681

682

683

684

685

686

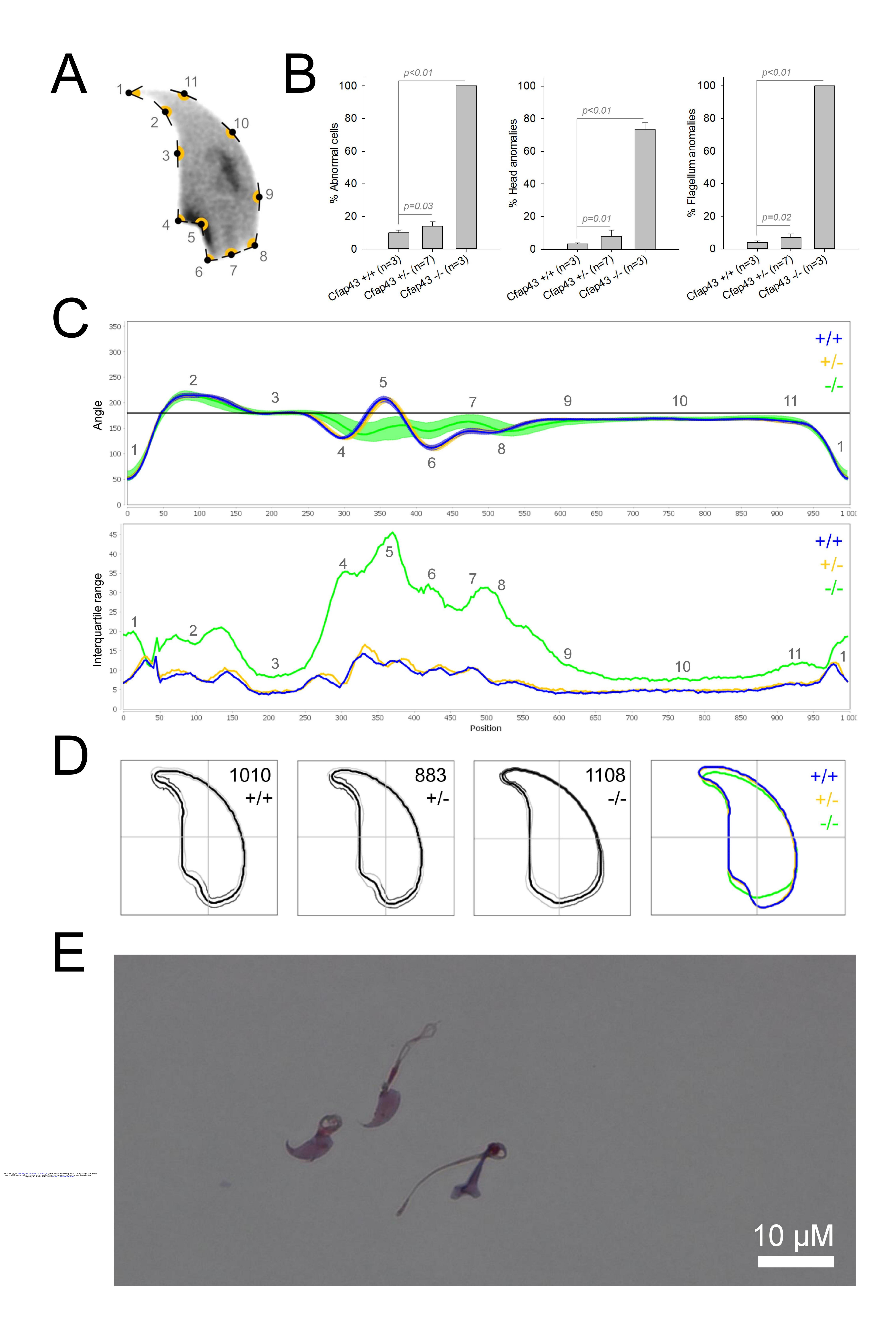
687

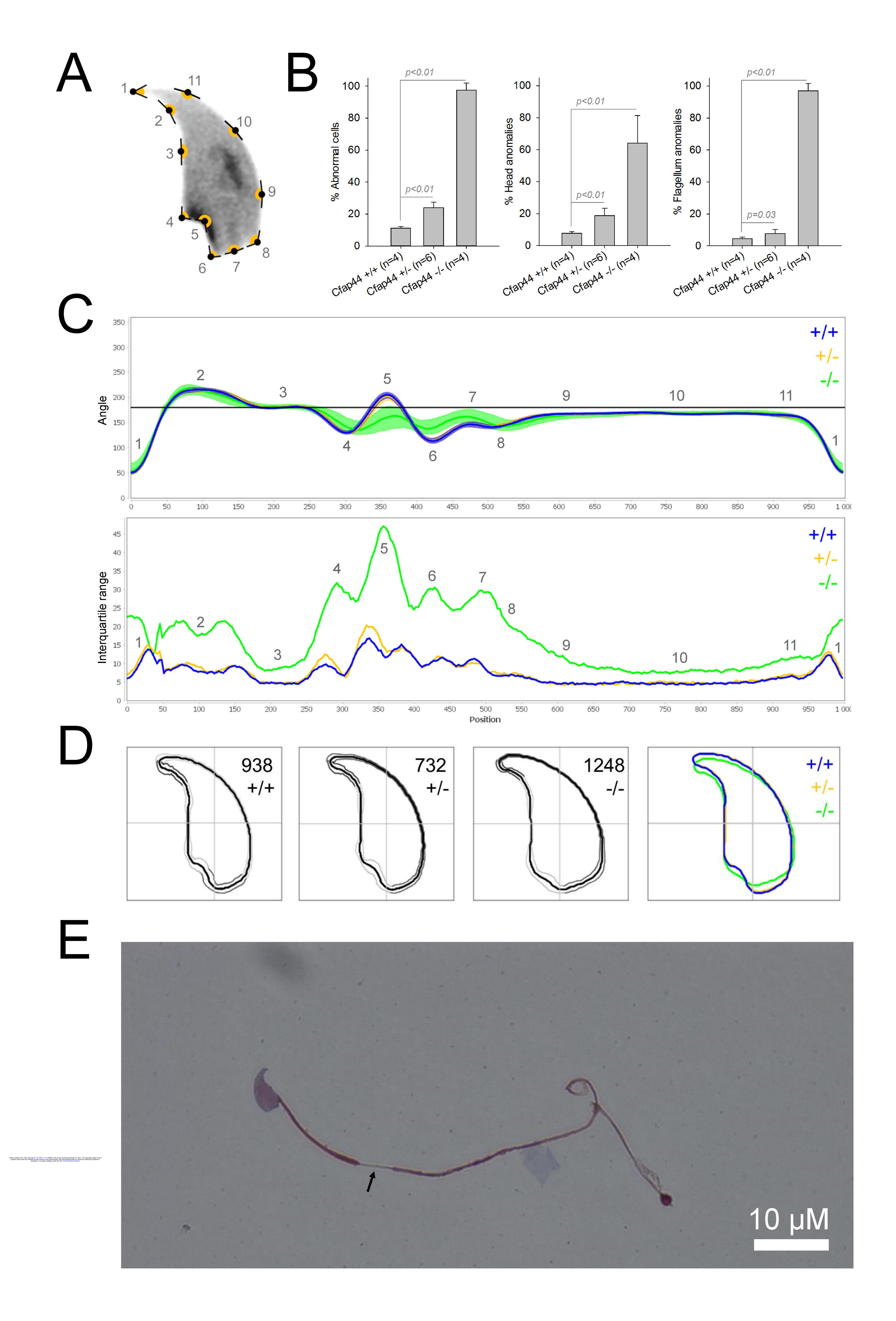
688

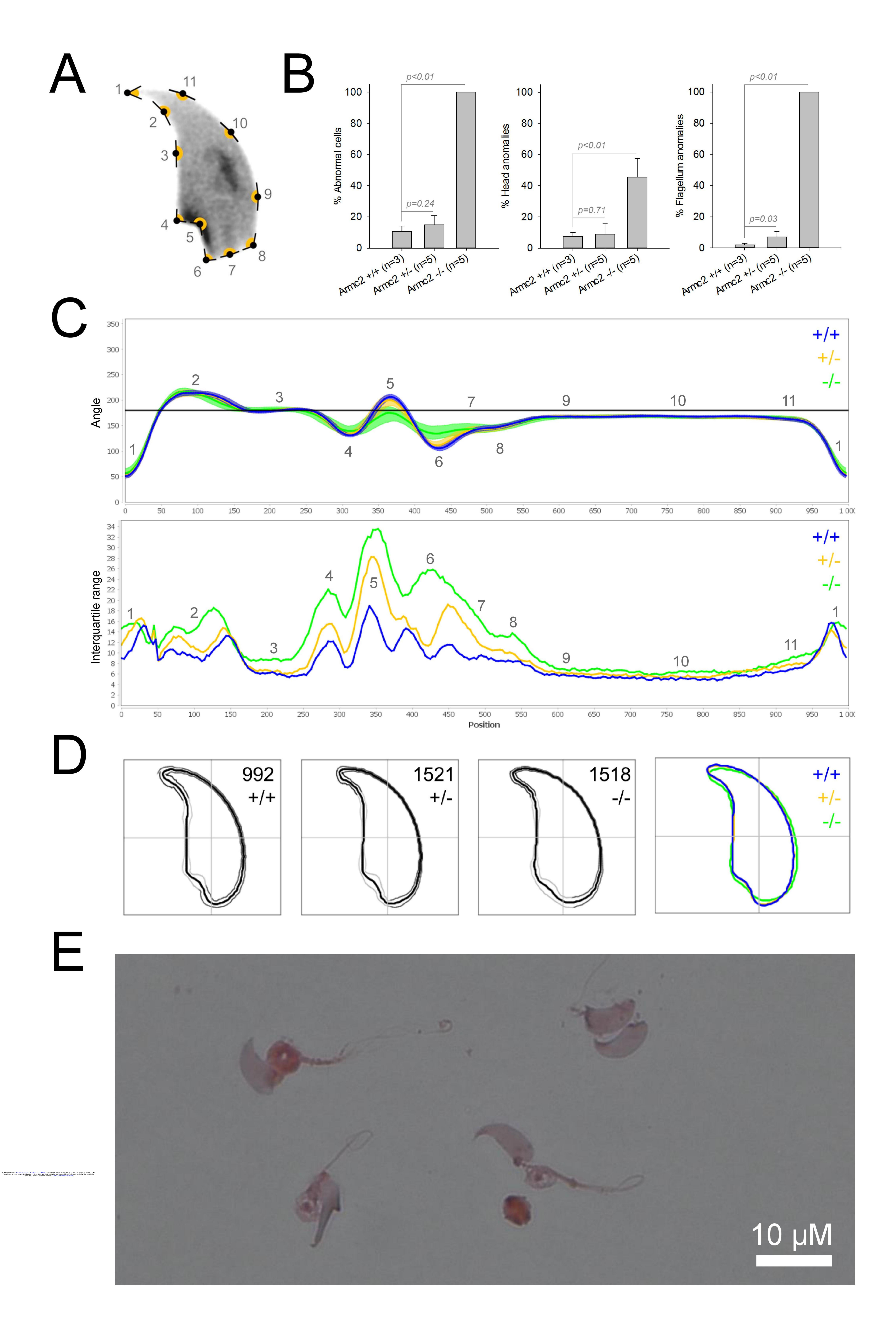
689

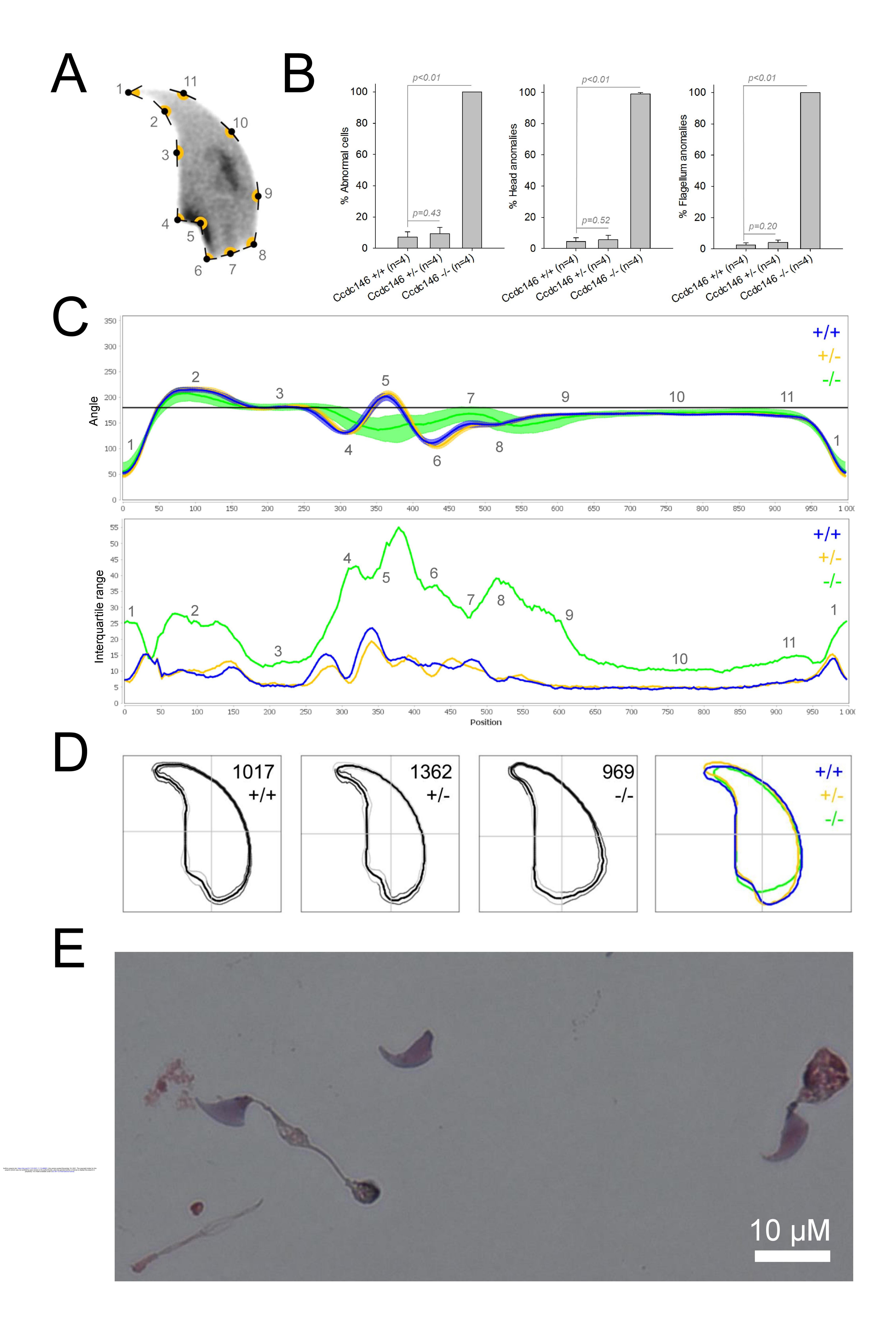
**Supplementary Figure 3.** Comparison of fine nuclear morphology for heterozygous animals produced during crosses of all strains. A. Consensus nuclear outlines for each strain alongside (blue=*Cfap43*, yellow=*Cfap44*, consensus nucleus green=Armc2, pink=Ccdc146). The numbers assigned to each consensus outline correspond to the number of nuclei processed per condition. **B.** Angle profiles for each strain focusing (black boxes) on positions of specific interest. The x axis represents an index of the percentage of the total perimeter, as measured counterclockwise from the apex of the sperm hook. The y axis shows the interior angle measured across a sliding window centered on each index location C. Variability profiles for each strain. The x axis is the same as for the angle profile, and the y axis represents the Interquartile Range (IQR) (the difference between the 75th and 25th percentiles). Specific regions of the nuclei are mapped on the profile and the graphical representation (from <sup>27</sup>) with: 1-tip; 2-under-hook concavity; 3-vertical; 4-ventral angle; 5-tail socket; 6-caudal bulge; 7-caudal base; 8-dorsal angle; 9-11-acrosomal curve. **Supplementary Figure 4.** Comparison of fine nuclear morphology for sperm heads from KO and WT animals. A. Consensus nuclear outlines for each KO strain alongside a merged consensus nucleus, and (far right) superimposition of the outlines of the four strains (blue=Cfap43, yellow=Cfap44, green=Armc2, and pink=Ccdc146). The numbers assigned to each consensus outline corresponds to the number of nuclei processed per condition. B. Angle profiles for each strain alongside an angle profile for wild-type mice (black), focusing (black boxes) on positions of specific interest. The x axis represents an index of the percentage of the total perimeter, as measured counterclockwise from the apex of the sperm hook. The y axis corresponds to the interior angle measured across a sliding window centered on each index location C. Variability profiles for each strain. The x axis is the same as for the angle profile, and the y axis represents the Interquartile Range (IQR) value (the difference between the 75th and 25th percentiles). Specific regions of the nuclei are mapped on the profile and the

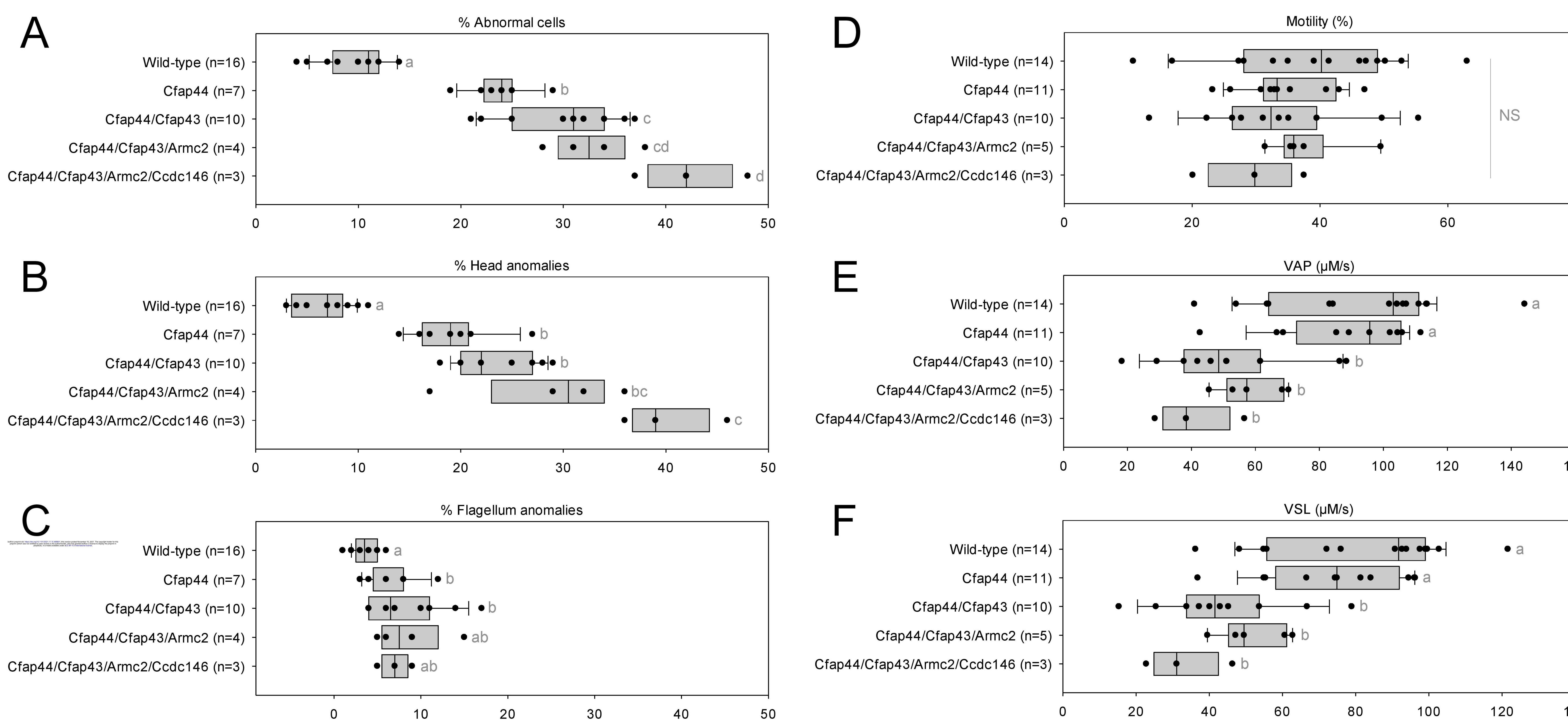
- 690 graphical representation (from <sup>27</sup>), with: 1-tip; 2-under-hook concavity; 3-vertical; 4-ventral
- angle; 5-tail socket; 6-caudal bulge; 7-caudal base; 8-dorsal angle; 9-11-acrosomal curve. **D.**
- Violin plots presenting mean data for representative nuclear parameters associated with each
- 693 gene. Statistical significance of differences between populations was assessed by the NMAS
- software, applying a Mann-Whitney U test. Significantly different populations are identified
- by distinct letters.
- 696 **Supplementary Figure 5.** Consensus and percentage distribution of the distinct sperm
- 697 populations classified based on nuclear morphology and according to the number of
- 698 heterozygous mutations.
- 699 **Supplementary Table 1.** Statistical data linked to the Student t-tests performed in figure 5A-
- 700 C. DoF = Degrees of Freedom; CI = Confidence Interval.
- 701 **Supplementary Table 2.** Statistical data linked to the Student t-tests performed in figure 5D-
- F. DoF = Degrees of Freedom; CI = Confidence Interval.
- 703 **Supplementary Table 3.** Statistical data linked to the Student t-tests performed in figure 6A-
- 704 C. DoF = Degrees of Freedom; CI = Confidence Interval.
- 705 **Supplementary Table 4.** Statistical data linked to the Student t-tests performed in figure 6D-
- 706 F. DoF = Degrees of Freedom; CI = Confidence Interval.
- **Supplementary Table 5.** Statistical data linked to the Student t-tests performed in figure 7A.
- 708 DoF = Degrees of Freedom; CI = Confidence Interval.
- **Supplementary Table 6.** Statistical data linked to the Student t-tests performed in figure 7B.
- 710 DoF = Degrees of Freedom; CI = Confidence Interval.

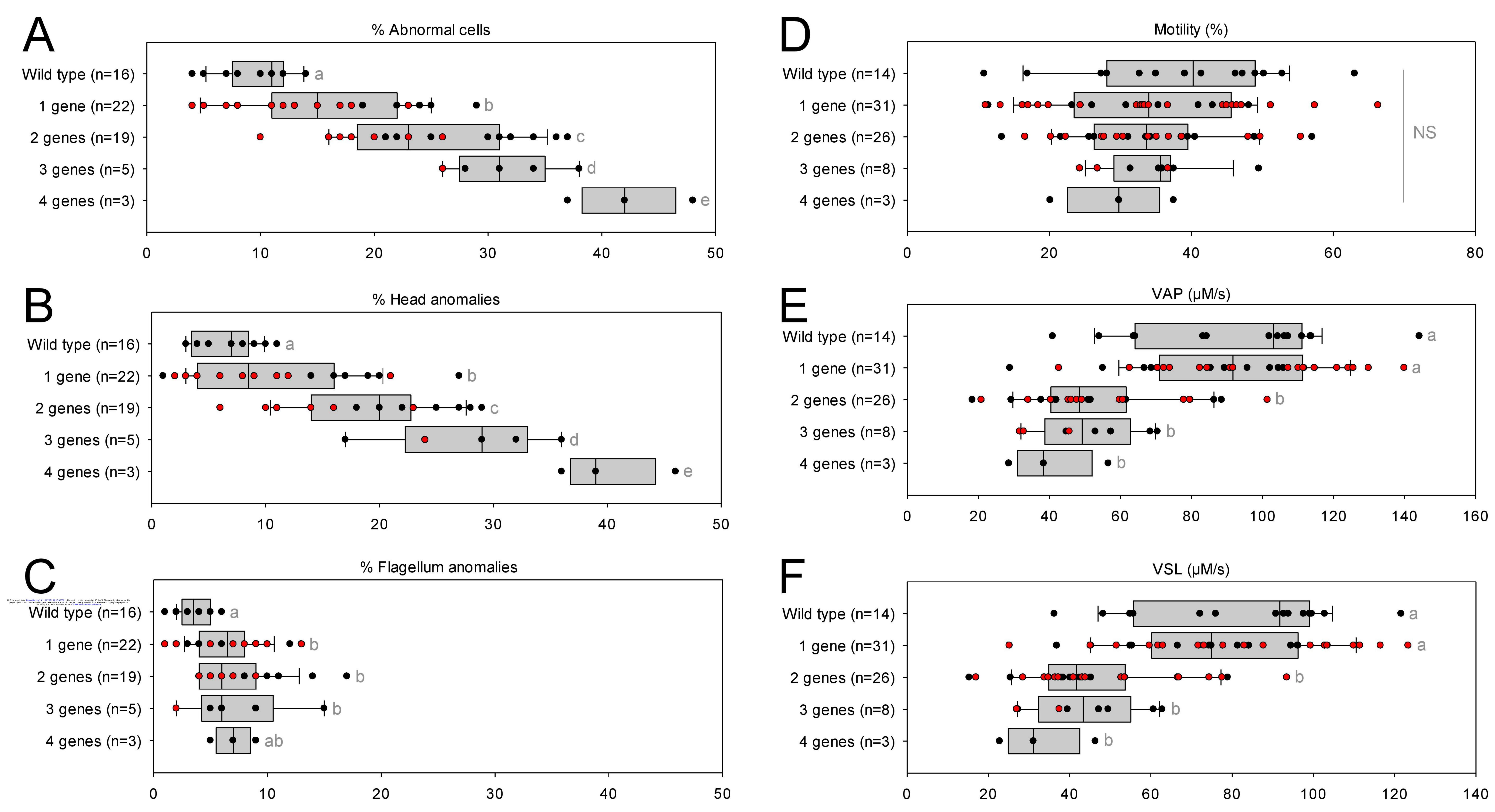


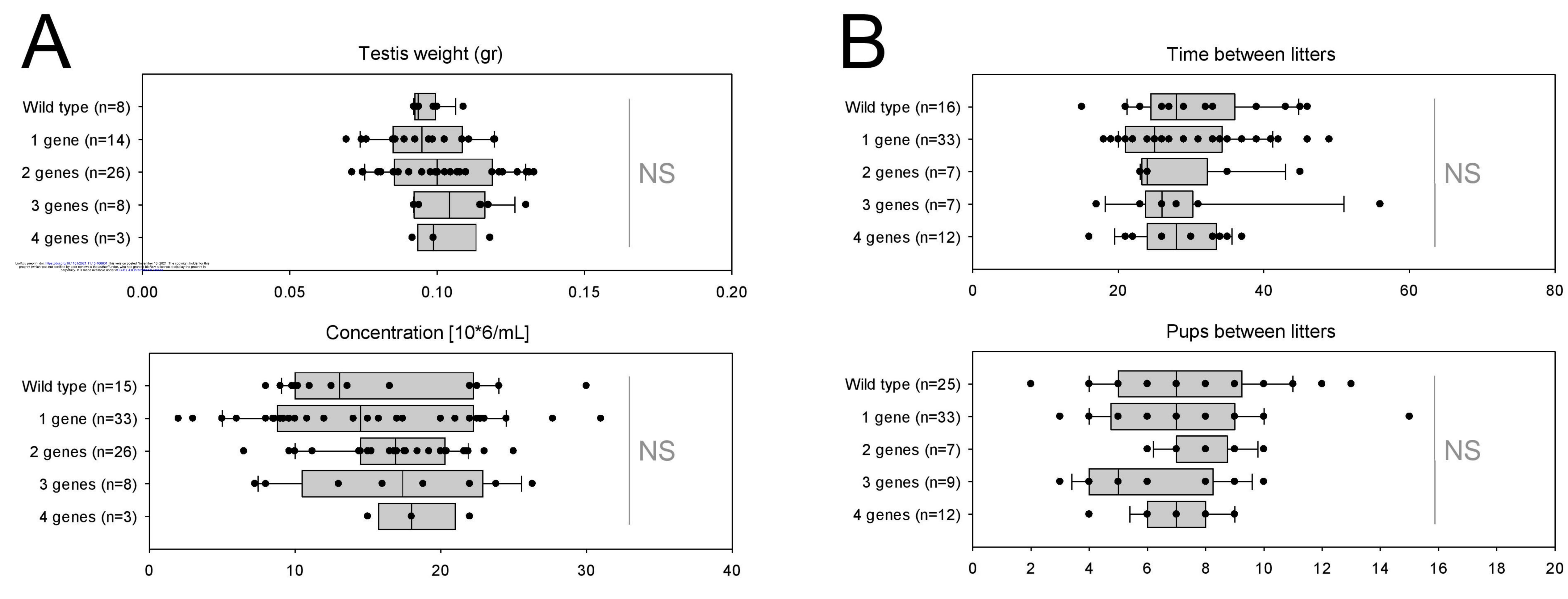


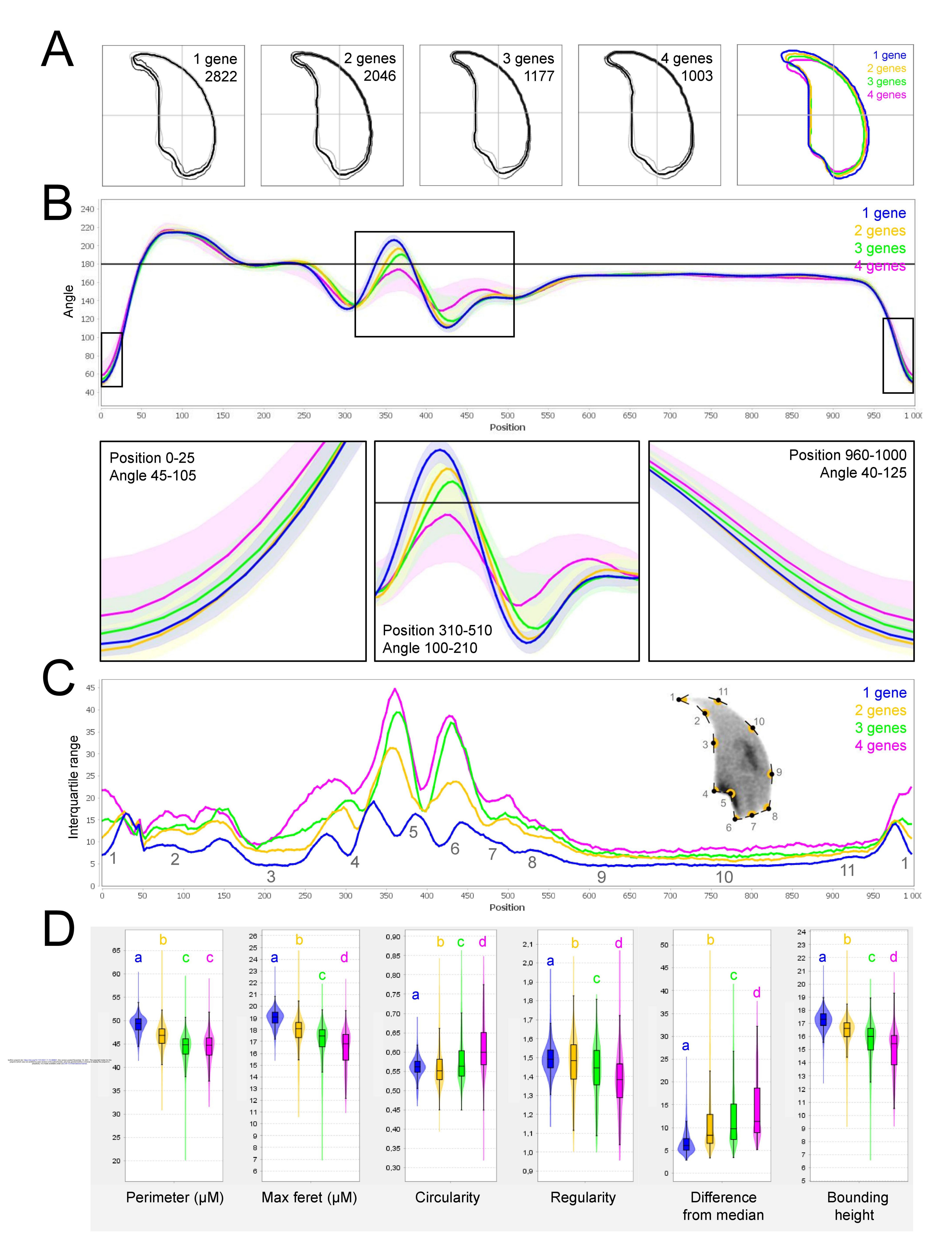


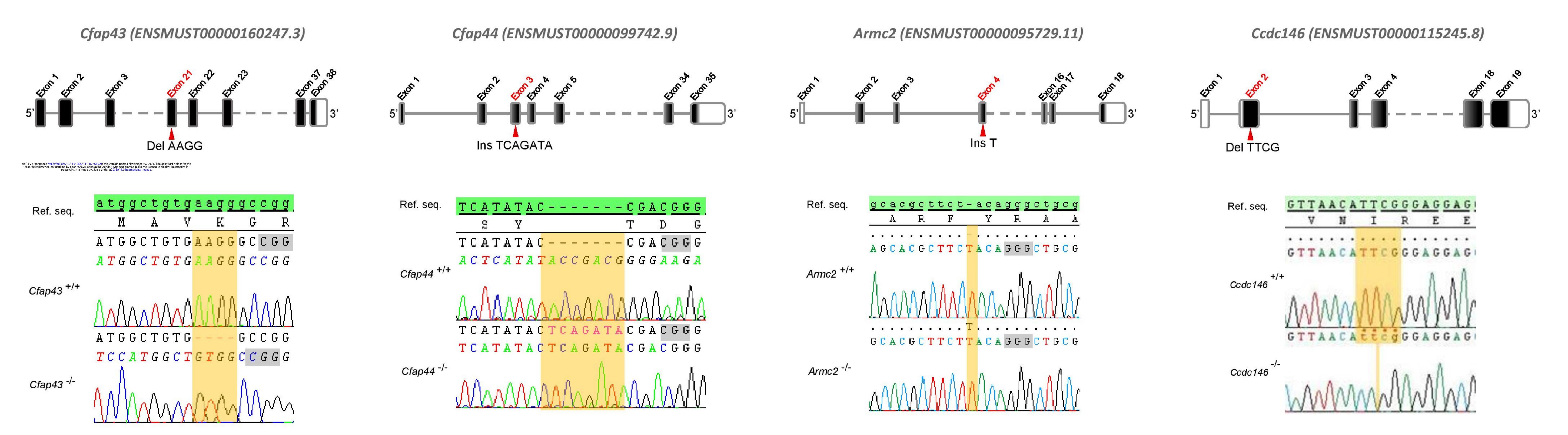


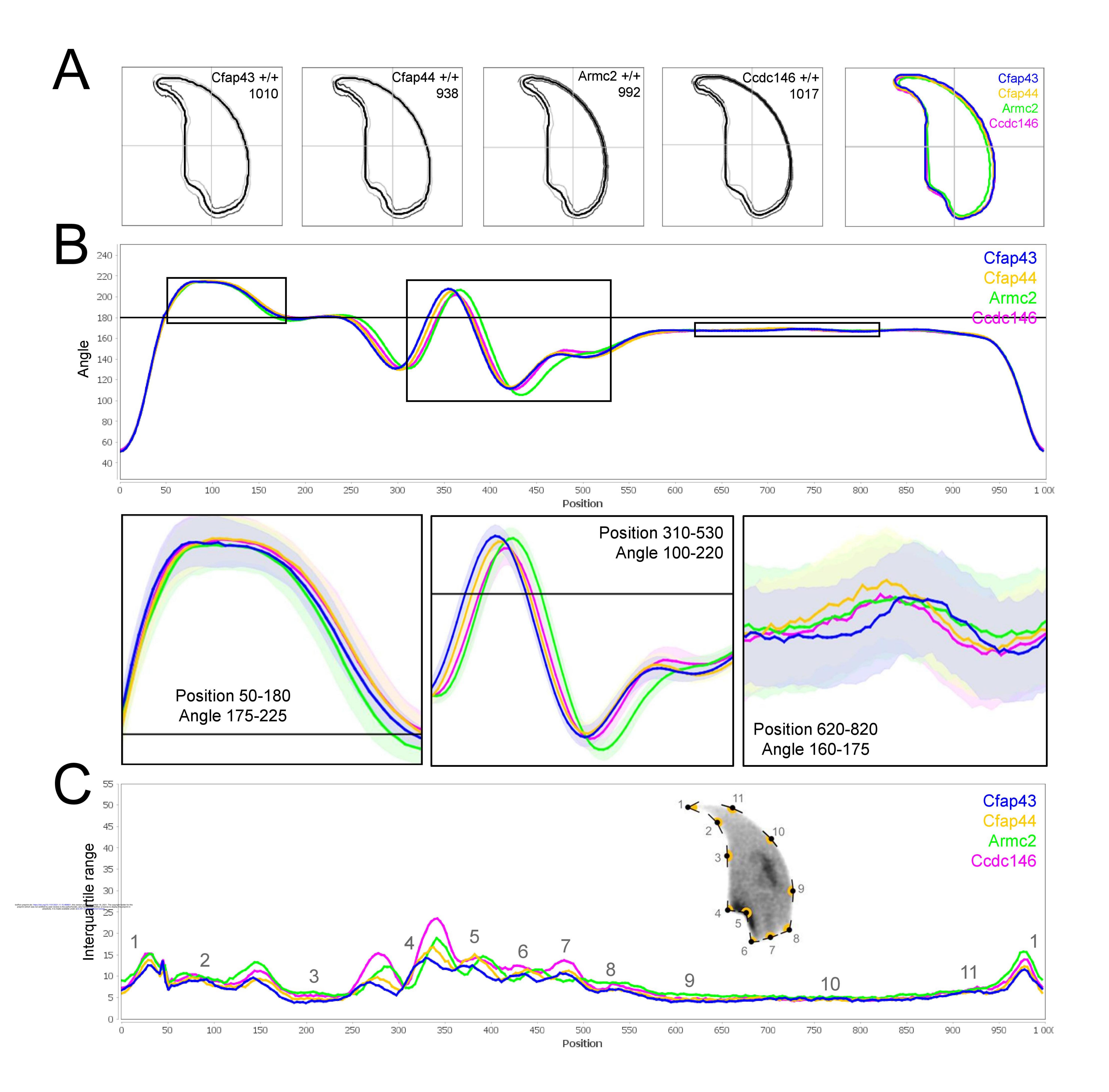


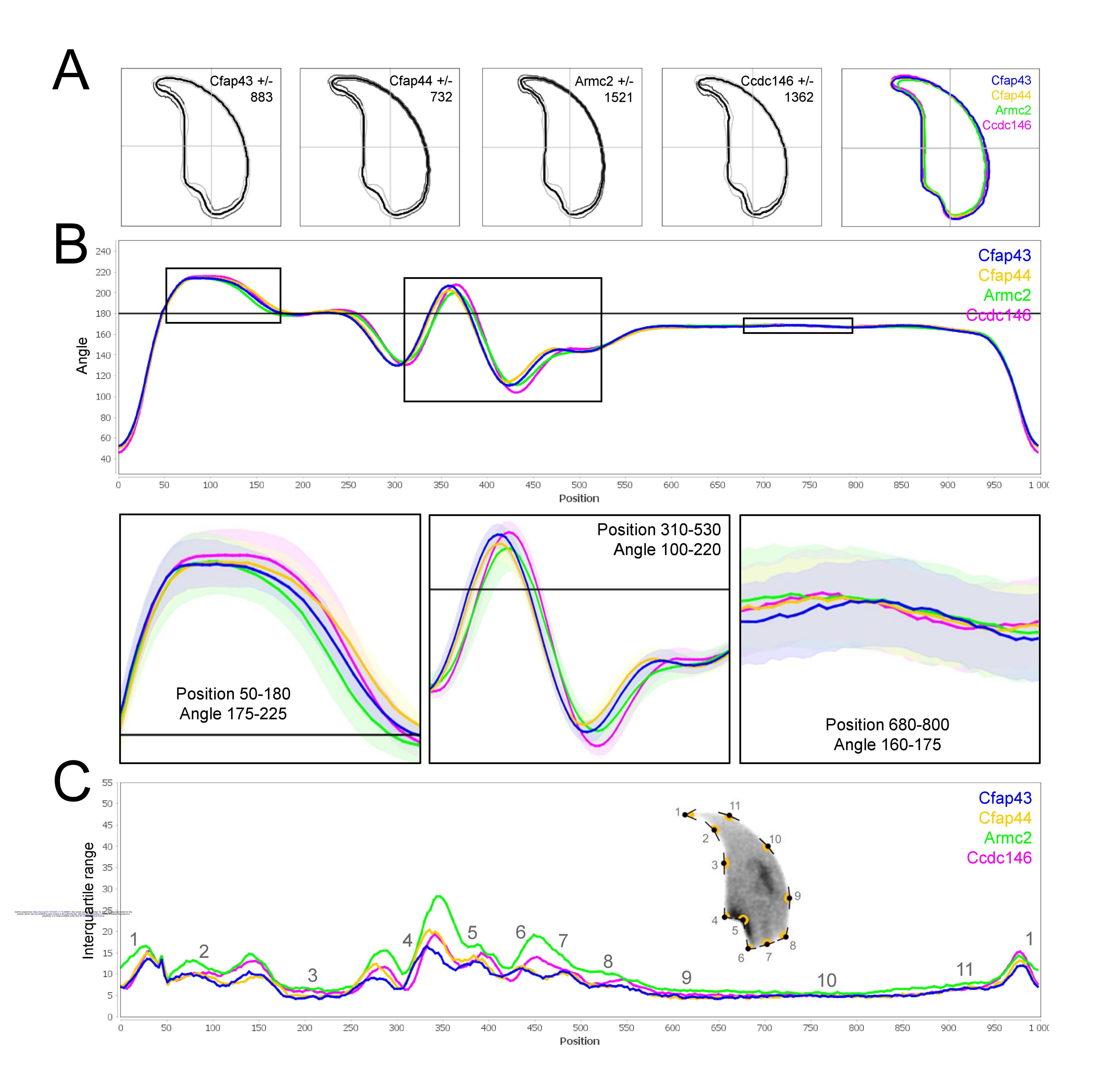


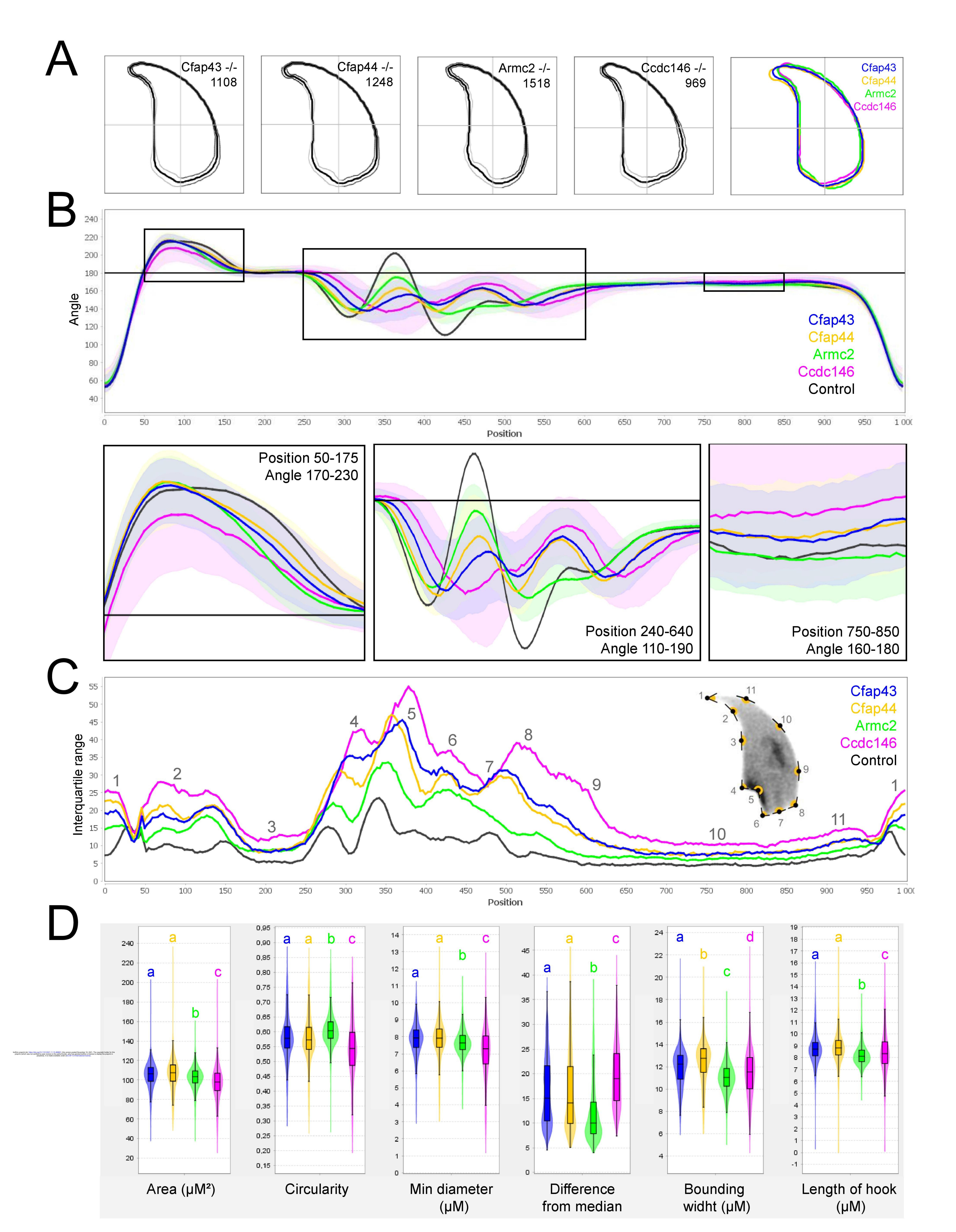












Consensus  bioRxiv preprint doi: https://doi.org/10.1101/2021.11.15.468601; this version posted November 16, 2021. The copyright holder preprint (which was not certified by peer review) is the author/funder, who has granted bioRxiv a license to display the prepertuity. It is made available under aCC-BY 4.0 International license.	r for this rint in										% abnormal cells
Head shape	Normal	Drop	Pepper	Claw	Sickle	Hammer	Cross	Cap	Lightning	Needle	
No mutation	98.33	0.53	0.00	0.82	0.07	0.18	0.00	0.00	0.00	0.07	1.67
One het. Mutation	95.55	1.48	0.11	1.83	0.30	0.34	0.11	0.04	0.04	0.19	4.45
Two het. Mutations	76.74	3.81	1.03	5.47	1.56	5.38	1.86	2.00	0.68	1.47	23.26
Three het. Mutations	66.60	6.54	3.02	5.53	1.81	6.74	2.92	2.31	1.31	3.22	33.40
Four het. mutations	44.71	3.35	6.26	8.53	3.24	7.34	10.04	4.64	3.13	8.75	55.29